RESEARCH ARTICLE | FEBRUARY 09 2026

Cislunar passive potential sensing through nonmonotonic sheath and ion wake barriers FREE

K. Champion ; H. Schaub

Phys. Plasmas 33, 023508 (2026)
https://doi.org/10.1063/5.0302512

Physics of Plasmas ARTICLE pubs.aip.org/aip/pop

Cislunar passive potential sensing through nonmonotonic sheath and ion wake barriers

Cite as: Phys. Plasmas **33**, 023508 (2026); doi: 10.1063/5.0302512
Submitted: 15 September 2025 · Accepted: 22 January 2026 ·
Published Online: 9 February 2026

K. Champion[a] and H. Schaub

AFFILIATIONS

Department of Aerospace Engineering Sciences, University of Colorado Boulder, Boulder, Colorado 80309, USA

[a]Author to whom correspondence should be addressed: kaylee.champion@colorado.edu

ABSTRACT

Knowledge of a neighboring spacecraft's potential in lunar orbit is critical for avoiding arc discharges during docking, accounting for electrostatic forces and torques, and evaluating lunar dust contamination risks. A servicing spacecraft can passively sense a target spacecraft's potential by measuring energies of naturally emitted electrons from the target. While this method has been explored for geosynchronous and cislunar applications, the effects of spacecraft ion wakes and nonmonotonic sheath formations have not been examined. These phenomena can create potential barriers that block emitted electrons, limiting the sensing signal. Barriers arise when the spacecraft width exceeds roughly half the electron Debye length. Wake-induced barriers persist for positive potentials while sheath-induced barriers persist for negative potentials. Large targets that generate such barriers produce lower detected current densities than smaller spacecraft under similar conditions. However, a positively charged servicer can still attract electrons, yielding a reduced but usable signal. The greatest limitation occurs when a target is in the wake of a highly positive servicer, leading to a highly negative target that repels ambient electrons and suppresses emissions. Mitigation strategies include avoiding this configuration or reducing the servicer's potential to shrink the wake.

I. INTRODUCTION

Spacecraft are exposed to space plasma, which generates surface currents and potentials on spacecraft through a process referred to as spacecraft charging. The magnitude of the surface potential is dependent on the local plasma parameters, sunlit surface area, material properties, and spacecraft geometry.[1] Thus, two spacecraft or electrically disconnected surfaces can charge differently in the same space environment, creating a myriad of issues during proximity operations. If the difference in potentials between two spacecraft surfaces is sufficiently large, an arc discharge can occur, frying components and potentially ending the mission.[2–6] This is dangerous during docking, particularly if one spacecraft is in the shadow of the other, as eclipsed spacecraft typically charge more negative than sunlit craft due to the lack of photoelectron emissions and ion flux.[7–9] Charged spacecraft can also exert electrostatic forces and torques on each other during proximity operations, which introduces unexpected perturbations that can require extra maneuvers and fuel to counteract.[10] In the cislunar regime, a lunar lander contaminated with regolith can contaminate the moon-orbiting vehicle it docks with. The surface potential of the ascending lander influences the lunar dust trajectories and contamination danger, as is shown with simulations of the Human Lander System docking with the Lunar Gateway.[11]

Knowledge of a nearby object's potential is critical for mitigating the dangerous effects of spacecraft charging during proximity operations. Touchless potential sensing techniques have been investigated to determine the potential of a neighboring spacecraft in Geosynchronous Earth Orbit (GEO) and cislunar environments. Active methods of touchless potential sensing involve a servicing spacecraft aiming an electron beam at a target spacecraft to excite secondary electron (SE)[12–15] and x-ray emissions,[16–18] or an ultraviolet (UV) laser to excite photoelectron emissions.[19] Passive methods rely on the x-ray and electron emissions naturally excited by the environment.[12,20–22] The flux of emissions measured by the servicer is typically lower for passive vs active sensing, but passive potential sensing is useful when active sensing methods may cause damage to sensitive components or induce unwanted charging. For all methods, the energy of the emissions is measured by the servicer and used to determine the potential of the target with respect to the servicer (Fig. 1). The servicer can determine its own potential using existing tools,[23–25] and the potential of the target is deduced.

Most of the touchless potential sensing research outlined in the previous paragraph has been conducted assuming GEO-like plasma conditions. In recent years, international enthusiasm for cislunar space has led to an increased number of missions, including Intuitive

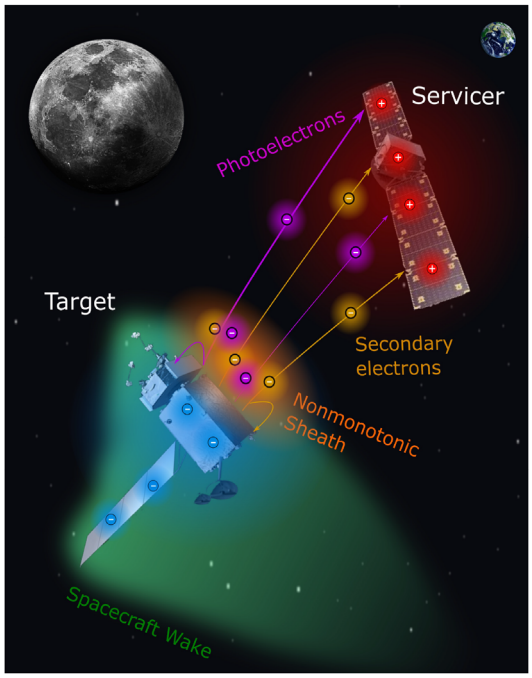

FIG. 1. Passive touchless potential sensing in cislunar space concept.

Machine's Odysseus spacecraft,[26] India's Chandrayaan-3 lander,[27] China's Chang'e-6 spacecraft,[28] and Japan's SLIM spacecraft.[29] Lunar Gateway is also currently being constructed by multiple partners around the globe and will provide a sustained human presence around the moon.[30] With more spacecraft and cislunar proximity operations, touchless potential sensing should be extended to cislunar space. However, plasma conditions in the cislunar solar wind and magnetosheath environment present new challenges for touchless potential sensing techniques, including shorter Debye lengths, spacecraft wakes, and nonmonotonic sheaths. The Debye length is a measure of how far a charge's electrostatic effect persists, and while touchless sensing is feasible despite short Debye lengths,[31] this is the first study to address the effects of wakes or nonmonotonic sheath formations on touchless potential sensing, which are not expected to form in the GEO environment.

This work aims to determine the conditions under which spacecraft wakes and nonmonotonic sheaths form around moon-orbiting spacecraft in the solar wind and their impact on electron emissions used for passive potential sensing. An overview of the environment and spacecraft–plasma interactions investigated is presented in Sec. II. The simulation setup in the spacecraft–plasma interaction software (SPIS) is presented in Sec. III. The spacecraft wake and nonmonotonic sheath formation are characterized for varying spacecraft sizes and surface potentials in Sec. IV. The impact of these formations on passive touchless potential sensing and the feasibility of passive potential sensing are investigated in Sec. V. Section VI presents the overview and conclusions of this work.

II. CISLUNAR ENVIRONMENT AND INTERACTIONS

The moon orbits through Earth's magnetosphere and out into the flowing solar wind, passing through a range of plasma environments. Several missions have helped characterize the cislunar plasma environments, including the Apollo missions,[32–34] the Wind spacecraft,[35] the Lunar Reconnaissance Orbiter (LRO),[36] and the twin Acceleration, Reconnection, Turbulence, and Electrodynamics of the Moon's Interaction with the Sun (ARTEMIS) spacecraft.[37] Measurements from the ARTEMIS spacecraft are analyzed and binned in the Design Specification for the Natural Environment (DSNE) document produced by NASA,[38] which identifies four plasma regions: solar wind, magnetosheath, magnetotail lobes, and plasma sheet. The solar wind is the plasma flowing from the sun and is located outside of Earth's magnetosphere in the interplanetary magnetic field.[39,40] The plasma sheet is a region of hot plasma in the Earth's magnetotail that magnetically maps to the auroral oval and splits the magnetotail into its top and bottom lobes. The plasma mainly consists of accelerated solar wind and can contain ionospheric ions when there is significant magnetospheric activity.[41] The magnetotail lobes are located within the magnetopause and mainly consist of plasma outflow from the ionosphere.[42,43] The magnetosheath is the transition region between the solar wind and magnetotail located between the bow shock and magnetopause.[44] The regions and interactions of Earth's magnetosphere and the cislunar environment are an active area of research; interested readers are referred to Refs. 45–47 for a more thorough review. Figure 2(a) depicts these regions using figures of the moon with respect to Earth's magnetic field. The magnetic field is shown in blue and the solar wind in light brown. In addition to orbiting through several regions, the moon alters the plasma environment. In the solar wind and magnetosheath, the moon absorbs and reflects plasma, leaving a low density, complex structure on the eclipse side of the moon, known as the lunar wake [Fig. 2(b)].[48]

Because of the different sources of plasma and interactions in each region, the magnetotail lobes and plasmasheet contain high-energy, low-density plasma, similar to the GEO environment, while the magnetosheath and solar wind consist of lower-energy, denser plasma. It is in these latter environments that spacecraft wakes and nonmonotonic sheaths are expected to form. The moon spends most of its orbit in the solar wind environment, so plasma parameters representative of solar wind plasma are implemented in this study. The conclusions can be extended to other environments in which spacecraft wake, and nonmonotonic sheath formations can be expected.

A. Spacecraft wakes

As a spacecraft moves through plasma, the ambient electrons and ions are pushed out of the way. In mesothermal plasma environments, the ion thermal velocity v_i is less than the velocity of the spacecraft with respect to the ambient plasma v_{sc}, which is less than the electron thermal velocity v_e ($v_i < v_{sc} < v_e$). Under these conditions, electrons catch back up to the spacecraft and impact on all sides, while the ions may take several spacecraft lengths to return to their undisturbed conditions, creating a complex region devoid of ions referred to as the spacecraft wake. Spacecraft wakes are investigated numerically to understand wake formations about spacecraft with large potentials,[49–51] their impact on surface charging,[7,52] and their effects on scientific instruments.[53–55] Spacecraft wakes have also been generated in vacuum chamber experiments to determine their properties,[56–61] characterize how wakes alter space plasma measurements,[62,63] and even investigate the effects of lunar wakes on regolith charging.[64]

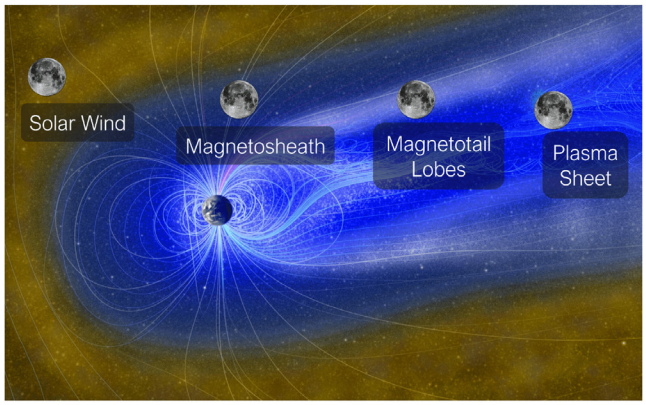

(a) Cislunar Environments (moon not to scale)

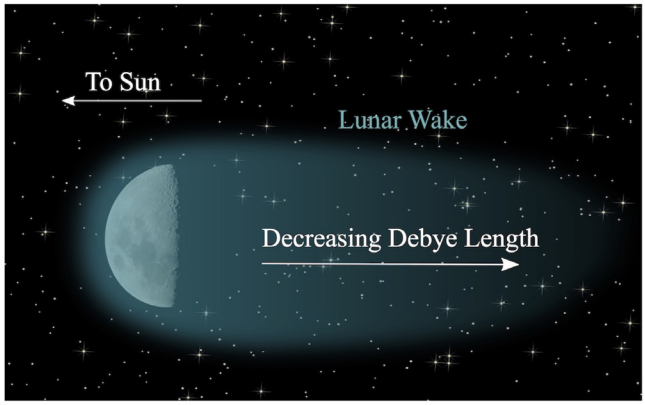

(b) Lunar wake

FIG. 2. Lunar plasma environments and interactions.[31] Reprinted with permission from Champion and Schaub, IEEE Trans. Plasma Sci. **51**, 2482–2500 (2023). Copyright 2023 IEEE.

Around the moon, spacecraft wakes are expected in the solar wind and magnetosheath regions.[65] On the dayside of the moon, the wake formation remains relatively consistent for varying spacecraft altitudes. On the eclipse side, spacecraft wakes are smaller near the surface, but as the craft's altitude increases, the wakes grow and eventually resemble the dayside wakes. In these regions, the solar wind is flowing from the Sun at velocities of several hundred kilometers per second, while the spacecraft orbits the moon with velocities on the order of one kilometer per second. Therefore, the wake always forms on the eclipse side of the moon, regardless of the direction of the spacecraft's velocity, as demonstrated in Fig. 3.

The shape and size of an ion wake depend upon several parameters, including the ion energy, bulk velocity, spacecraft size, spacecraft potential, and Debye length. The Debye length in a Maxwellian plasma is given by

$$\lambda_D = \sqrt{\frac{\varepsilon_0 T_e}{n_e q_e}}, \tag{1}$$

where ε_0 is the permittivity of free space, T_e is the electron temperature in eV, q_e is the elementary charge, and n_e is the undisturbed electron density. A Maxwellian distribution is commonly used to represent cislunar plasma.[11,66–68] Recent work has also indicated that a Kappa distribution, which has a higher energy tail than the Maxwellian distribution, is appropriate to approximate cislunar plasma distributions.[22,69,70] The inclusion of a Kappa distribution is outside the scope of this work.

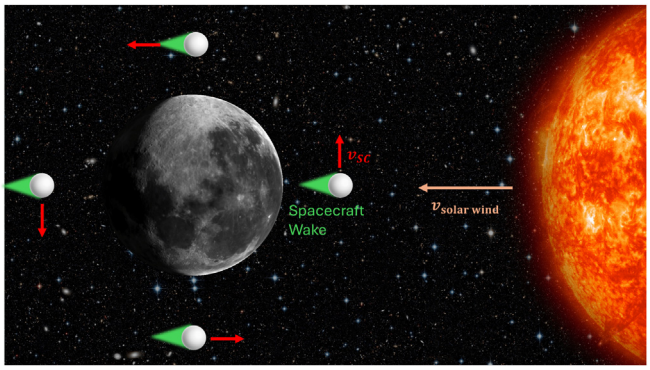

FIG. 3. Cislunar spacecraft ion wake formations.

A *narrow wake* forms with a width approximately equal to the spacecraft's width W_{SC} when the ion bulk flow energy E_{bulk} is greater than the magnitude of the spacecraft potential $q_e\phi_{SC}$. The bulk flow energy in eV is

$$E_{\text{bulk}} = \frac{m_i v_{\text{bulk}}^2}{2q_e}, \tag{2}$$

where m_i is the ion mass and v_{bulk} is the bulk velocity of the plasma. If the spacecraft potential becomes more positive than the ion flow energy and the Debye length is larger than the spacecraft width ($m_i v_{\text{bulk}}^2/2 < q_e\phi_{SC}$, $\lambda_D > W_{sc}$), an *enhanced wake* formation can occur. In this formation, the ions are deflected around the points where the potential $\phi(r)$ is equal to the ion flow velocity instead of the spacecraft body, and a significantly wider wake can form. Conversely, if the magnitude of a negative spacecraft's potential is larger than the ion flow velocity and the Debye length is comparatively large ($m_i v_{\text{bulk}}^2/2 < -q_e\phi_{SC}$, $\lambda_D > W_{sc}$), a *focused wake* can form with a width much smaller than the spacecraft width.[63,71–73]

In wake formations in which the Debye length is much larger than the spacecraft, the changes in the potential field are averaged out over the width of the wake. In other words, the wake size is increased or decreased when the spacecraft becomes more positively or negatively charged, but changes to the potential due to the absence of ions in the wake are averaged out and are negligible. If the spacecraft width is larger than the Debye length, the wake is less significantly altered by changes in the spacecraft potential, but the wake can create negative potentials due to the absence of ions.[74] This negative potential field can create a barrier that low energy electron emissions cannot get through, but the magnitude of this barrier as a function of spacecraft size and potential has not been investigated.

B. Nonmonotonic sheaths

In a typical spacecraft sheath, the potential decreases monotonically from the spacecraft surface value to zero. In this scenario,

low-energy electron emissions, such as secondary electron and photoelectron emissions, can return to the surface if the spacecraft is positively charged, as shown in Fig. 4(a). Conversely, if the spacecraft is charged negatively, the electron emissions should be repelled from the spacecraft's surface.

When electrons are emitted, their negative charge reduces the potential field. Once the ratio of emitted electrons to incoming electrons Γ reaches some critical value Γ_c, the electrical field above the surface becomes zero, and a space-charge-limited (SCL) sheath is formed. The electrons then are not accelerated away from the spacecraft surface and settle a short distance away, typically characterized by the photoelectron λ_{ph} or secondary electron λ_{SE} Debye length. Further electron emissions then cause the potential to dip below the spacecraft surface potential. Figure 4(b) shows an example of a nonmonotonic potential sheath above a positive spacecraft. This sheath formation can occur as a result of photoelectron and/or secondary electron emissions, and the critical ratio Γ_c can be approximated as[75]

$$\Gamma_c = 1 - 8.3\sqrt{\frac{m_e}{m_i}}, \tag{3}$$

where m_e is the mass of an electron, and m_i is the ion mass. The nonmonotonic sheath is also a barrier that can prevent low-energy electron emissions from leaving the spacecraft surface, effectively reducing the emitted electron yield. If the ambient electron energy is greater than the electron emission energy, as would be expected in the cislunar solar wind, the current reduction of electron emissions is greater than the reduction of incoming electron current and the spacecraft charges more negatively than expected.

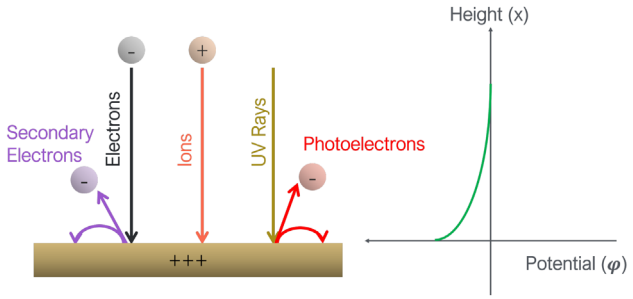

(a) Monotonic

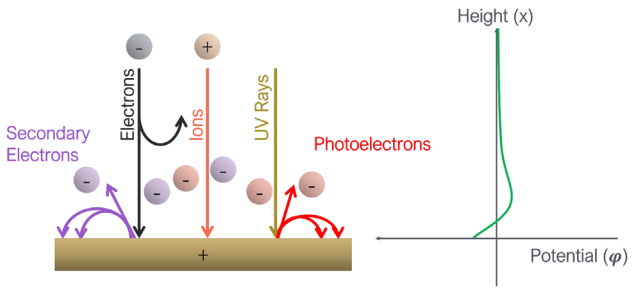

(b) Nonmonotonic

FIG. 4. Schematic of monotonic and nonmonotonic sheath formation for a positively charged, sunlit spacecraft.

In addition to having a large emitted to incoming electron ratio, the spacecraft size must be comparable to or larger than the photoelectron and electron Debye lengths for nonmonotonic sheaths to form. The photoelectron Debye length is typically much smaller than the electron Debye length and dominates near the spacecraft surface, while the electron Debye length dominates farther from the spacecraft. If the spacecraft is comparable in size to the electron Debye length and much larger than the photoelectron Debye length, the *thin sheath* approximation applies. In this regime, a nonmonotonic sheath creates a potential barrier close to the spacecraft surface. If the spacecraft is much smaller than the Debye length, the *thick sheath* approximation applies, and the barriers effectively disappear. In this regime, recollection of electron emissions is driven by positive surface potentials attracting emitted electrons instead of the nomonotonic sheath.

Nonmonotonic sheaths have been investigated both analytically and numerically to determine their impact on spacecraft charging,[76–78] scientific measurements,[79,80] and lunar surface charging.[66,81,82] Experimental results have validated their formation,[83,84] and they have been observed above the dayside lunar surface[21] and about the HELIOS spacecraft.[85] However, a complete characterization of nonmonotonic sheath formation as a result of the spacecraft size to Debye length ratio and spacecraft surface potential has not been presented.

III. SIMULATION SETUP

Simulations are conducted in spacecraft plasma interactions software (SPIS), a spacecraft plasma interaction software created by the Spacecraft Plasma Interactions Network in Europe (SPINE).[86] Two environments are modeled in SPIS: solar wind dayside and solar wind eclipse at an altitude greater than 12 000 km. The environment parameters are based on the mean environments given in the DSNE and presented in Table I.[38]

For simulations with floating spacecraft, the surface potential is determined by solving the current balance equation

$$I_i(1+\delta_i) - I_e(1-(\eta+\delta)) + I_{ph} = 0, \tag{4}$$

where I_i and I_e are the incident ion and electron currents, respectively, and I_{ph} is the photoelectron current. The variables η, δ, and δ_i are the backscattered electrons, secondary electrons from electrons and secondary electrons from ions, respectively. The photoelectron and secondary electron emissions from ambient electron currents are utilized

TABLE I. Simulation environment parameters.[38]

Parameter	Solar wind dayside	Solar wind eclipse >12 000 km
Particle density ($n_e = n_i$)	6×10^6 m^{-3}	2.5×10^6 m^{-3}
Electron temperature (T_e)	11 eV	19 eV
Ion temperature (T_i)	7 eV	66 eV
Debye length (λ_D)	10.1 m	20.5 m
Plasma bulk velocity (v_{bulk})	420 km/s	400 km/s
Photoelectron current density (J_{ph})	4×10^{-5} A/m^2	N/A
Max SE yield (δ_{max})	0.97	1.25
Energy at max SE yield (E_{max})	300 eV	135 eV

for touchless potential sensing, so they are described here for convenience.

The secondary electron yield δ is defined in SPIS using a four-parameter fit[87,88]

$$\delta(E) = R_1 E^{e_1} + R_2 E^{e_2}, \tag{5}$$

where R_1 and R_2 are in Angstroms, and e_1 and e_2 are unitless inputs used when defining the material. The fitting parameters are 154, 220, 0.8, and 1.76 for R_1, R_2, e_1, and e_2, respectively, based on the values for aluminum-2k in SPIS. The maximum yield δ_{max} and electron energy at which the maximum yield occurs E_{max} for each environment are shown in Table I. For all scenarios, the ions are assumed to be protons, H^+, so the critical ratio at which a nonomonotonic sheath can form using Eq. (3) is approximately 0.81. The solar wind is approximately 95% protons, 4% alpha particles (He^{++}) and 1% other ions,[39,40] so simulating the ion population using protons is an appropriate assumption. If ion mass is approximated using a ratio of 95% protons and 5% alpha particles, the critical ratio is still approximately 0.81. The δ_{max} and E_{max} parameters are selected such that δ is less than Γ_c in the dayside plasma and greater than Γ_c in the eclipse plasma. This causes a nonmonotonic sheath due to secondary electrons to form in the eclipse environment and a nonmonotonic sheath due to photoelectrons to form in the dayside environment and allows the different types of sheath formations to be evaluated independently of each other. The main difference between the photoelectron and secondary electron sheaths is the density of the two emissions (photoelectron density is typically larger) and the regions around the spacecraft in which the sheaths form. Photoelectrons are only emitted on the sunlit side of the spacecraft, while secondaries may be emitted from all faces.

The photoelectron number density n_{ph} is

$$n_{ph} = \frac{2J_{ph}}{q_e v_{ph}}, \tag{6}$$

where J_{ph} is the photoelectron current density, $v_{ph} = \sqrt{2q_e T_{ph}/(\pi m_e)}$ is the photoelectron velocity, and T_{ph} is the photoelectron temperature. Both photoelectron and secondary electron emissions are assumed to have an energy of 2 eV and a Maxwellian distribution. The photoelectron number density is then approximately 1054 cm^{-3}, and the photoelectron Debye length λ_{ph} using Eq. (1) is 0.32 m.

The computational space is defined using a tetrahedral mesh created in Gmsh and loaded directly into the *Mesh* tab in SPIS. A 0 V Dirichlet boundary condition is implemented, and the external boundary is set far enough from the spacecraft to allow the potential to naturally reach zero before reaching the boundary (typically $\approx 6\,\lambda_D$). On the spacecraft surface, the resolution is 0.15 m, about half the photoelectron Debye length. A charging simulation with a 0.1 m mesh size on the spacecraft surface showed a negligible difference in results while significantly increasing the computational time. The external boundary resolution is 5 m in the solar wind dayside and 10 m in the solar wind wake environment, about half the respective Debye lengths.

Open boundaries are defined for the particles, which means particles can be injected and lost through the surface. The electrons and ions are modeled using the particle-in-cell (PIC) option, where macroparticles are generated and tracked throughout the computational space. All electron emissions are also modeled with PIC to capture the complex dynamics near the spacecraft surface. When conducting PIC simulations, the time-steps must be small enough to ensure stability and smooth convergence, and the ions should not travel more than one mesh tetrahedral in each time step.[89] The maximum integration time for all particles is set to 1×10^{-6} s, approximately the time it takes the ions to cross the smallest mesh tetrahedral. The total run time is at least 2×10^{-4} s, the time it takes the ions to cross the entire computational space. If the simulation has not converged within this time, meaning the surface potentials and currents are still changing, the computational time is extended. The steady state is typically achieved between 3×10^{-4} and 5×10^{-3} s, and the run time is between 3 and 48 h using a 32 GB RAM desktop, depending on the scenario simulated.

IV. SINGLE SPACECRAFT CHARACTERIZATION

A. Floating spacecraft

The solar wind cislunar environment is unique because it is possible for smaller spacecraft to be in the thick sheath regime, while nearby

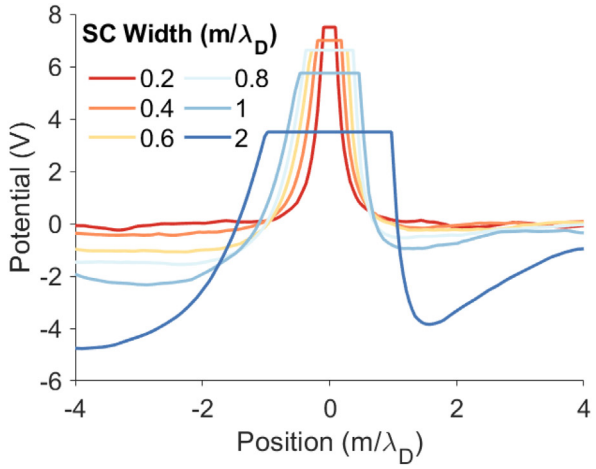

(a) Dayside

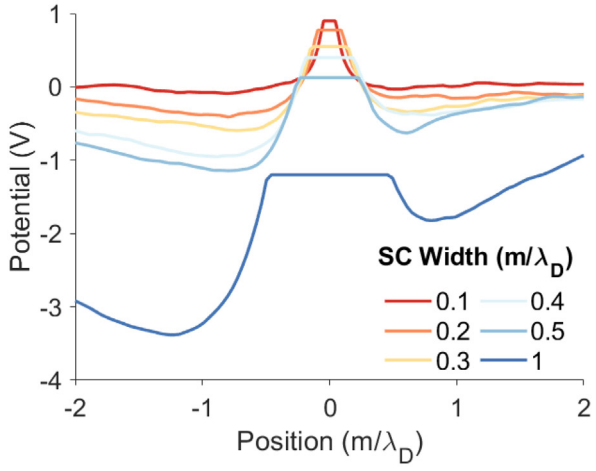

(b) Eclipse

FIG. 5. Potential fields about spacecraft of varying widths in the dayside and eclipse environment. Positive and negative x values indicate the ram and wake side of the spacecraft, respectively.

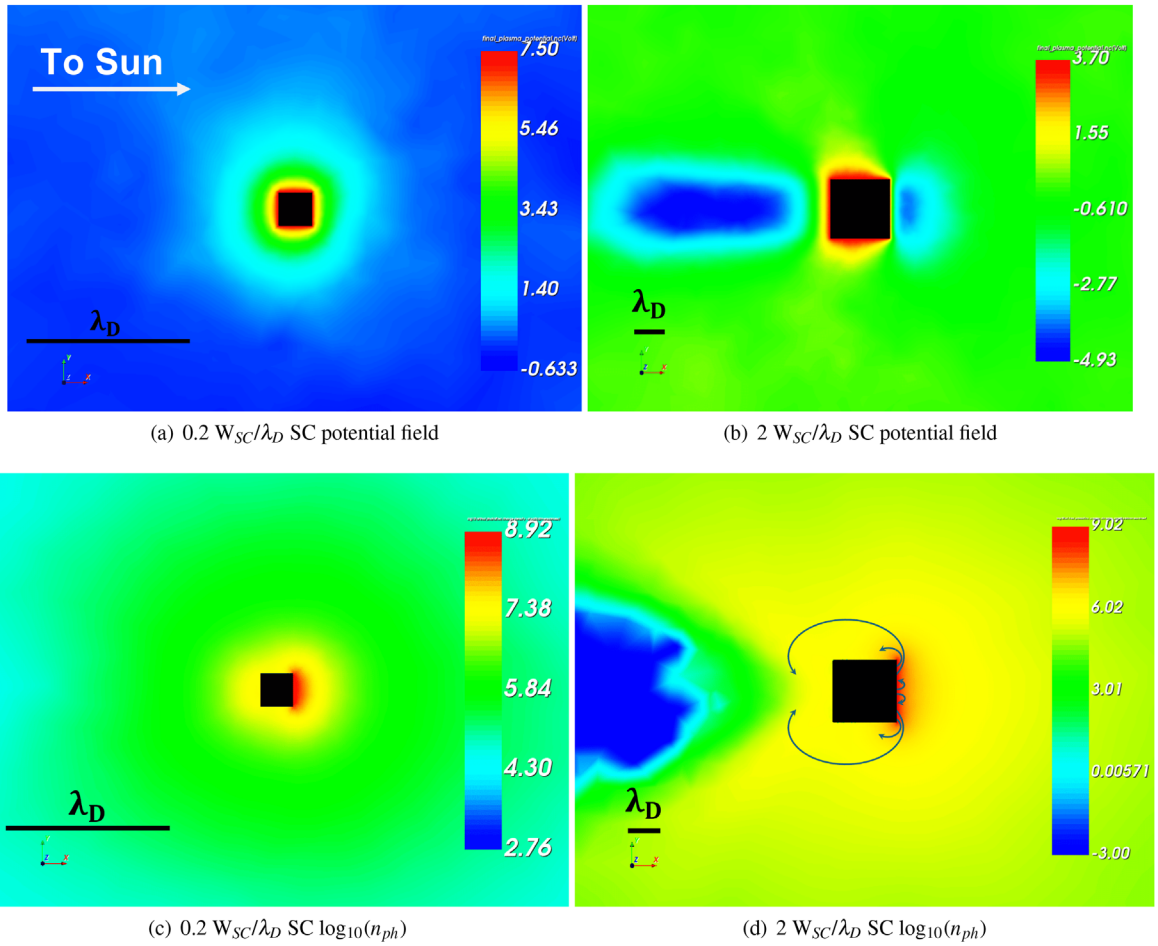

(a) 0.2 W_{SC}/λ_D SC potential field

(b) 2 W_{SC}/λ_D SC potential field

(c) 0.2 W_{SC}/λ_D SC $\log_{10}(n_{ph})$

(d) 2 W_{SC}/λ_D SC $\log_{10}(n_{ph})$

FIG. 6. The potential field (top) and $\log_{10}$ of the photoelectron density n_{ph} (bottom) around a 0.2 W_{SC}/λ_D (left) and 2 W_{SC}/λ_D (right) spacecraft in solar wind dayside plasma.

larger spacecraft can be in the thin sheath regime. Therefore, it is necessary to determine the spacecraft width to Debye length ratio at which the regime transitions from thick to thin sheath and barriers due to spacecraft wakes and nonmonotonic sheaths may be expected to form. This is first done using floating cubic spacecraft of varying widths to provide insight into when the barriers form and how they impact the charging behavior of the spacecraft.

Figure 5 shows the resulting potential fields about the floating spacecraft with varying width to Debye length ratios ρ. As ρ increases, barriers due to the wakes and nonmonotonic sheaths begin to form. In the dayside environment, the nonmonotonic sheath begins to form due to photoelectron emissions on the ram side of the spacecraft (positive x-values in Fig. 5) when ρ is 0.8. On the wake side, the ion wake begins to influence the potential field and create a barrier when ρ is 0.6. As ρ increases beyond these values, the size of the barrier increases, preventing more electron emissions from leaving the spacecraft surface and driving the spacecraft more negative. This trend is also seen for the spacecraft in the eclipse environment, but barriers begin to form on the ram and wake side of the spacecraft when ρ is 0.4 and 0.2, respectively. The secondary electron emissions on the wake side may increase the barrier size at lower ρ values. In addition, the spacecraft potential magnitudes are lower in this region, and the relationship between the spacecraft potential and barrier formation is explored in Sec. IV B.

The difference in potential field and photoelectron trajectories for a spacecraft in a thick and thin sheath regime in the dayside environment is demonstrated in Fig. 6. When the spacecraft is much smaller than the Debye length (thick sheath), the potential decreases monotonically to zero as the distance from the spacecraft surface increases, and the photoelectrons create a *photoelectron sheath* around the body. When the spacecraft is larger, barriers due to the spacecraft wake and photoelectron nonmonotonic sheath are observed. The minimum potential in the nonmonotonic sheath occurs approximately 5 m from the spacecraft surface, about half a Debye length. This allows some photoelectrons to escape around the sides of this barrier; however, the wake prevents photoelectrons from entering the wake side of the spacecraft, creating an empty region in the photoelectron sheath. These interpreted electron trajectories are shown in Fig. 6(d) as navy arrows to help the reader visualize the description.

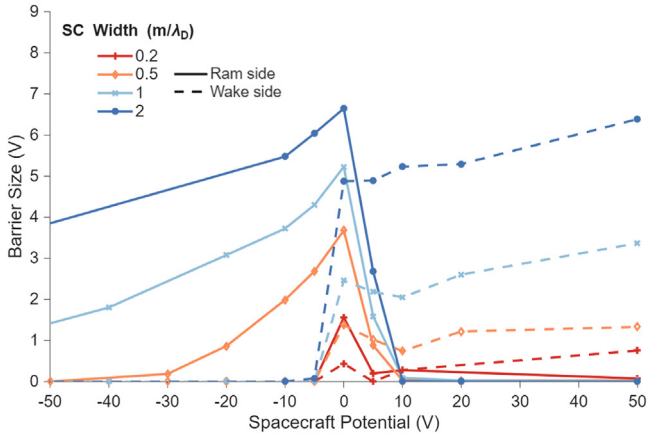

(a) Dayside

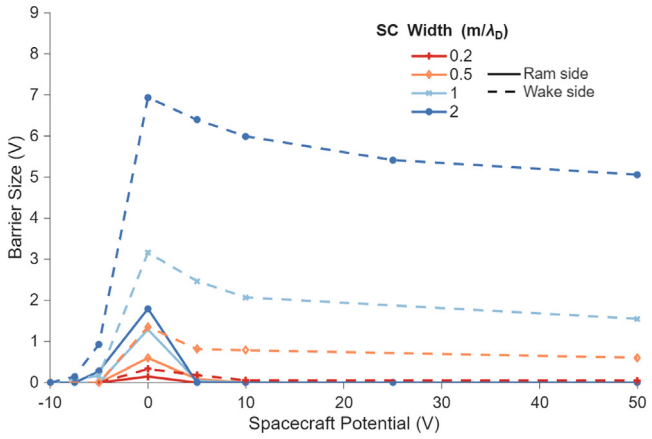

(b) Eclipse

FIG. 7. Barrier size on the wake and ram side of a constant potential spacecraft on the dayside (left) and eclipse side (right) of the moon.

B. Constant potential

In Sec. IV A, barriers formed for smaller ρ values in the eclipse environment than in the dayside environment. However, the floating spacecraft potentials are smaller in eclipse, indicating that there is likely a relationship between the spacecraft potential and barrier size. There is precedence for this; Thiébault *et al.*[90] show that if a spacecraft becomes more than a couple of volts positive, the electron emissions are attracted back into the surface and the barrier disappears. However, the relationship between negative spacecraft potentials and the barrier formation has not been established, and varying spacecraft size in the same environment has not been considered.

The size of the barrier ϕ_{barrier} for this evaluation is considered to be

$$\phi_{\text{barrier}} = \phi_{\text{min}} - \phi_{SC} \quad \text{for} \quad \phi_{\text{SC}} < 0, \tag{7a}$$

$$\phi_{\text{barrier}} = -\phi_{\text{min}} \quad \text{for} \quad \phi_{\text{SC}} > 0, \tag{7b}$$

where ϕ_{min} is the minimum potential and ϕ_{SC} is the surface potential of the spacecraft. Typically, a positive spacecraft potential is considered as part of the barrier ($\phi_{\text{barrier}} = \phi_{SC} - \phi_{\text{min}}$ for $\phi_{SC} > 0$) as a positive spacecraft also draws electron emissions back into the spacecraft. For this study, barriers due to nonmonotonic sheaths and spacecraft wakes are isolated from the spacecraft potential.

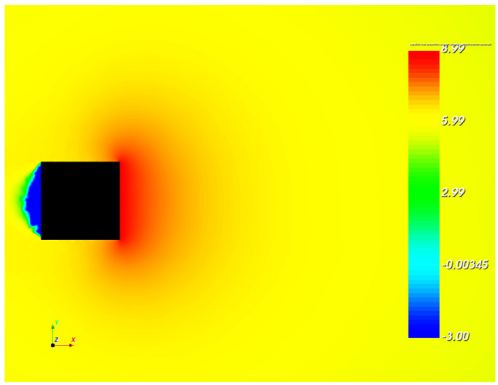

(a) 0 V

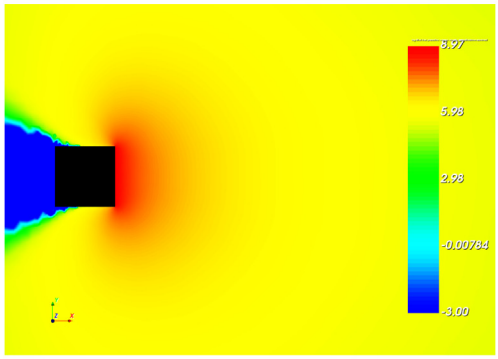

(b) -5 V

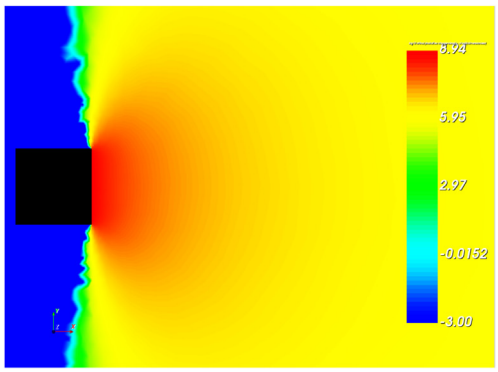

(c) -20 V

FIG. 8. Log_{10} of the photoelectron density about a $0.5\,W_{SC}/\lambda_D$ width spacecraft in the solar wind dayside region at various surface potentials.

Figure 7 shows the barrier sizes on the wake and ram side of spacecraft of varying widths and surface potentials on the dayside and eclipse side of the moon. As observed with floating spacecraft, the larger the spacecraft becomes, the larger the barriers become. For all

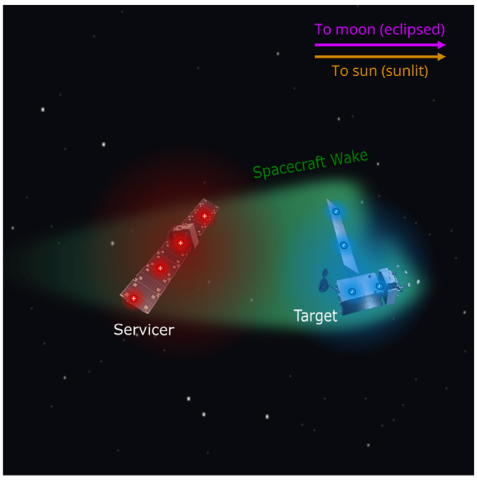

(a) Servicer in wake

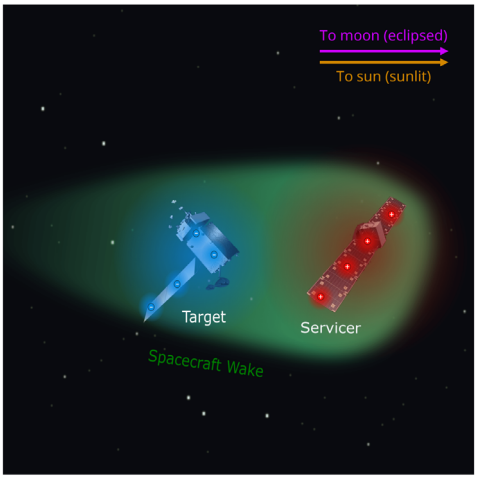

(b) Target in wake

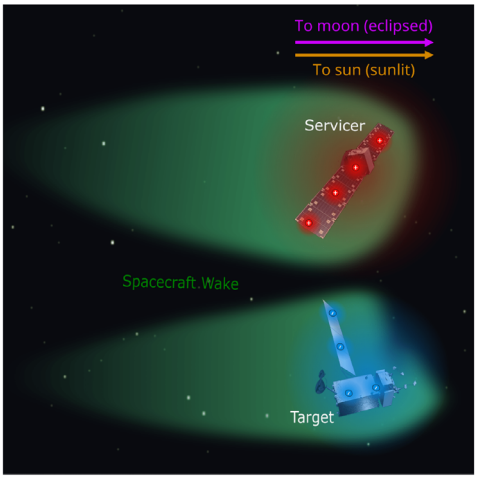

(c) Parallel wakes

FIG. 9. Spacecraft positions for touchless potential sensing simulations.

spacecraft sizes, once a spacecraft becomes a couple volts positive, the electron emissions are attracted back into the spacecraft surface, and the nonmonotonic sheath and associated barriers disappear, matching the results from Ref. 90. It is possible that a small barrier exists within one mesh element in the simulation and not captured for more positive potentials than indicated. At this point, the size of the barrier is likely smaller than 2 eV, the mean energy of the electron emissions, and the recollection of electron emissions is driven by the positive spacecraft potential more than the barrier.

The nonmonotonic barriers on the ram side persist for larger negative spacecraft potentials. The reason for this is twofold. When the spacecraft becomes more negative, the electron emissions are more effectively repelled, decreasing Γ near the surface of the craft. In addition, the electron emissions are accelerated, increasing the T_e value for the photoelectron or secondary electron Debye length from Eq. (1). This causes the emissions to spread out and settle farther from the spacecraft, decreasing the barrier size. Figure 8 demonstrates this, as the red region of dense photoelectrons spreads farther from the spacecraft as the surface potential gets more negative. In addition, the dark blue region, indicating an absence of photoelectrons, becomes larger as the spacecraft gets more negative. At smaller potential magnitudes, the photoelectron emissions can nearly surround the spacecraft and generate the photoelectron sheath [see Fig. 6(c)]. As the spacecraft becomes more negative, it increasingly repels and accelerates the photoelectrons away from the surface (toward the right in Fig. 8), decreasing the photoelectron emissions' ability to surround the spacecraft. This further indicates that the electron emissions are more efficiently repelled as the spacecraft becomes more negative. This process is not as efficient as recollecting the emissions with a positively charged spacecraft, so the barriers persist for more negative potentials. Larger barriers around bigger spacecraft also require more negative potentials to dispel the electron emissions. This causes the larger barriers from photoelectrons to persist for larger negative potentials than the smaller barriers from secondary electrons. It is again possible that a barrier smaller than one mesh element persists for more negative potentials than indicated, but the barrier size is most likely smaller than the energy of the emitted electrons.

The barriers on the wake side of the spacecraft disappear for small negative potentials and persist for larger positive potentials. This follows the trend for spacecraft wake formations, as large negative spacecraft potentials create a focused wake while large positive potentials create an enhanced wake. However, it is surprising that the barrier due to the wake disappears for negative spacecraft potentials of less than ten volts because the ion flow energy is 919.1 and 833.6 eV in the dayside and eclipse environment, respectively. This may be attributed to the process in which the wake creates a barrier in contrast with the nonmonotonic sheath. The barrier size of the wake when the spacecraft is uncharged is less than ten volts for the spacecraft sizes simulated, and it is likely that the barrier size in the wake remains constant. Then, once the spacecraft is more negative than the barrier, there is no longer a noticeable dip in the potential field. This also explains the trend for the wake side barrier about positive spacecraft, as the barrier remains close to its initial value as the spacecraft charge becomes more positive. As a reminder, at highly positive potentials, the spacecraft's surface potential attracts the majority of secondary electron and photoelectron emissions back into its surface. So in this region, the electron emissions are already expected to be repressed, but the wake may

TABLE II. Passive sensing results.

Servicer potential (V)	SC width (m/λ_D)	Position	Target potential (V) (Sun/Eclipse)	Frac. of emissions recollected (Sun/Eclipse)	Detected emissions (A/m^2) (Sun/Eclipse)
300	0.2	Servicer in wake	90/6.5	0.6/0.082	1.9×10^{-6}/2.2×10^{-6}
300	1	Servicer in wake	42.5/7	0.73/0.13	3.6×10^{-7}/2.1×10^{-6}
300	0.2	Parallel wakes	33.75/5.4	0.8/0.13	1.1×10^{-6}/2.3×10^{-6}
300	1	Parallel wakes	18/5.0	0.85/0.12	3.6×10^{-7}/1.4×10^{-6}
300	0.2	Target in wake	−70/−25	0/0	0/7.5×10^{-8}
300	1	Target in wake	−100/−32.5	0/0	0/6×10^{-8}
50	0.2	Servicer in wake	32.5/3.0	0.81/0.16	5.0×10^{-6}/9.4×10^{-7}
50	1	Servicer in wake	13/1.3	0.87/0.18	2.1×10^{-6}/8.3×10^{-7}
50	0.2	Parallel wakes	31.5/3.0	0.86/0.1	2.4×10^{-6}/6.3×10^{-7}
50	1	Parallel wakes	9.5/1.8	0.89/0.1	6.1×10^{-7}/4.0×10^{-7}
50	0.2	Target in wake	−32.5/3.3	0/0.14	5×10^{-9}/9.4×10^{-7}
50	1	Target in wake	−32.5/−2.3	0/0.017	1×10^{-8}/6.5×10^{-7}
0	0.2	Target in wake	−23/1	0/0.1	1.25×10^{-8}/1.5×10^{-7}
0	1	Target in wake	−14.25/−2.75	0/0.036	3×10^{-8}/1.75×10^{-7}

further prevent electrons from entering the wake-side region about the craft, as demonstrated in Fig. 6.

To review, as the spacecraft becomes larger, the barrier size due to the spacecraft wake and nonmonotonic sheath increases, reducing the floating spacecraft potential. When holding the spacecraft at a constant potential, the barriers are largest when the spacecraft potential is smaller, and the width is larger, persist in the wake for more positive potential, and persist in the nonmonotonic sheath for more negative potentials. In general, the barrier only exceeds 2 eV (the electron emission temperature) when the spacecraft width to Debye length is at least 0.5. Therefore, when the spacecraft width is smaller than this, barrier formations can largely be ignored, and barriers become more consequential as the spacecraft width gets larger.

V. PASSIVE POTENTIAL SENSING SIMULATIONS

Passive potential sensing simulations are conducted to determine how barriers impact sensing and the conditions in which the servicer detects more emissions from the target. Based on the results in Sec. IV, there are four sensing environments defined: (1) sunlit with a barrier ($W_{SC} = 1\,\lambda_D$), (2) sunlit without a barrier ($W_{SC} = 0.2\,\lambda_D$), (3) eclipse with a barrier ($W_{SC} = 1\,\lambda_D$), and (4) eclipse without a barrier ($W_{SC} = 0.2\,\lambda_D$). The servicer and target are the same size in all simulations and have a separation distance of one spacecraft width.

In each environment, three relative spacecraft positions are simulated: servicer in target's wake, target in servicer's wake, and parallel wakes as shown in Fig. 9. A constant potential servicer and floating potential target are modeled to determine how the servicer's potential changes the target's potential, emitted current, and detected current. Potential control of one's own spacecraft could be achieved through technologies such as biasing of electric field sensors,[91] electron gun emissions,[92–94] and ion emissions.[95–98] In all environments and relative positions, the servicer is held at 50 and 300 V. A 50 V servicer is highly likely to be more positive than the target, allowing it to attract emitted electrons. A 300 V servicer will draw in electron emissions and attract and accelerate the ambient electrons, which may then impact the target with energy closer to E_{max} and increase the secondary electron yield. E_{max} is commonly between 280–800 eV for spacecraft surface materials, so a servicer potential of several hundred Volts could reliably increase the yield from a variety of targets.[99,100] A more positive servicer is not used because increasing the ambient electron energy significantly past E_{max} results in less detected current.[31] As a worst-case scenario, a 0 V servicer is also modeled with the target in the servicer's wake, as this is the only orientation where it is likely that the target is charged negatively. The target's electron emissions that impact the side of the servicer facing the target are considered detected for touchless potential sensing, and emissions from the servicer are set to zero to ensure that servicer's own emissions are not falsely recorded as current for touchless potential sensing.

A. Characterization results

Table II and supporting Fig. 10 show the relevant passive potential sensing results. When the target is not in the servicer's wake, it charges more positively than the individual spacecraft charged in Sec. IV A because the servicer is drawing electron emissions away from the target, effectively increasing its emissions current. In addition, when the target is larger, it is seen that generally its potential is more negative, more current is recollected, and less current density is detected by the servicer. This follows expectations, as larger spacecraft are expected to have larger barriers. However, several of the target potentials are greater than ten volts positive, so nonmonotonic sheaths would not be expected to form. The difference in behavior can be explained by the size of the spacecraft relative to the photoelectron, secondary electron, and electron Debye lengths. For the larger spacecraft, the electron emissions settle closer to the target surface, and the positive servicer's potential does not reach as far around the target. Both of these make it more difficult for the servicer to pull electron emissions away from the target for sensing. Figure 11 demonstrates this, as a higher density of photoelectrons travels farther from the smaller target's surface.

Regardless of size, when the servicer is more positive, and the target is not in the servicer's wake, the target charges more positively, and less emissions are recollected. This occurs because the more positive

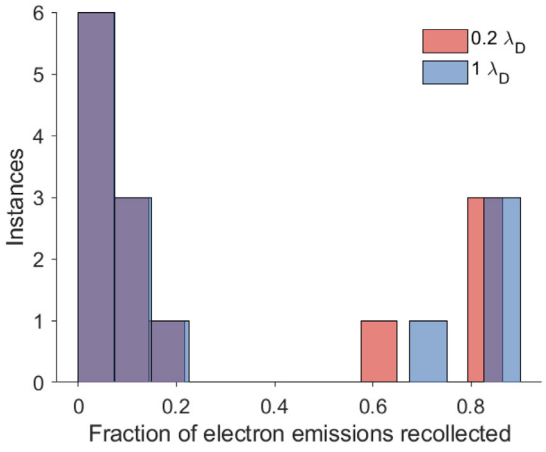

(a) Emission recollection vs size

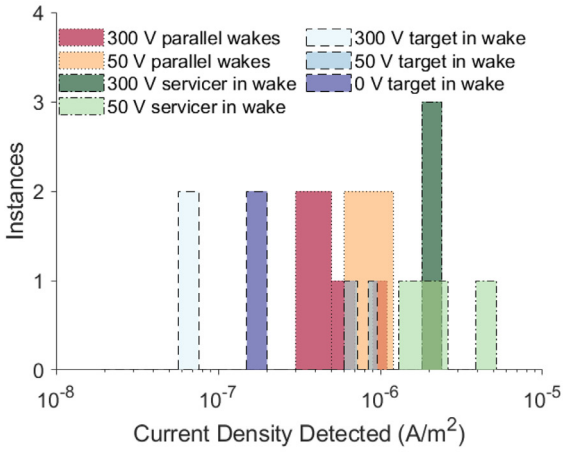

(b) Detected current density vs servicer position and potential

FIG. 10. Passive potential sensing results breakdown.

servicer may increase the ambient electron energy closer to E_{max} and draws more electron emissions away from the target. For the eclipsed spacecraft, this corresponds to a higher detected secondary electron current density. For the sunlit spacecraft, the higher potential servicer detects *less* current density. In this case, the photoelectron emissions are significantly larger than the secondary electron emission, and the initially generated photoelectron current density does not vary with the target's potential. So, the photoelectron trajectories due to the spacecraft potentials are the main factors in the amount of detected current, not the secondary electron yield. Bengtson *et al.*[12] previously showed that a lower magnitude target potential is better for touchless potential sensing. When a more positive servicer generates a more positive target, the electron emissions are more influenced by the electric field about the target than the attractive force exerted by the servicer. This is demonstrated in the top two images of Fig. 11, where the photoelectron emissions are drawn nearly directly into the surface of the 50 servicer facing the target, while the emissions seem to orbit the 300 V servicer. Therefore, when the target is not in the servicer's wake, a 50 V servicer is better when detecting photoelectron emissions, and a 300 V servicer is better when detecting secondary electron emissions.

For both spacecraft sizes and in both the sunlit and eclipse environment, the servicer detects the most current when it is in the wake of the target. This is interesting because the wake is expected to serve as a barrier around a positively charged, larger target. Instead, the positive servicer is able to "punch through" barriers around the target and draw electron emissions in. This can be seen in Fig. 11, as the photoelectron emissions are drawn away from the target in all scenarios shown. Furthermore, the photoelectrons are present even in the regions to the right of the spacecraft where the wake barrier is expected, contrary to what is seen in Fig. 6(d), where the photoelectrons are repelled by the negative potential in the wake.

The discussion so far has only addressed results when the target is not in the servicer's wake. When the target is in the servicer's wake, the target generally charges negatively, little to no electron emissions are recollected, and the detected current is lower than the other two orientations. Notably, no electron emission is detected when the servicer is 300 V positive. This occurs because the electron flux to the target exceeds the ion flux in the wake and charges the target negatively. At the floating potential, the negatively charged target repels the ambient electrons, as shown in Fig. 12. It should be noted that an intermediate $20 \times 20 \times 20$ m meshing grid with a resolution of 0.5 m is utilized to increase the resolution of the image. No changes are observed in the results when the intermediate meshing grid is implemented. Because the electrons are repelled from the target, they cannot create secondary electron emissions, so there is nothing to sense. While the wakes are classified as *narrow wakes* for all tested servicer potentials, the 50 and 0 V servicer has slightly smaller wakes than the 300 V servicer, increasing the target's ion current and final potential. Electrons can then reach the more positive target and generate secondary electrons, albeit at a lower magnitude than in the other tested positions. Therefore, it is best to avoid putting the target in the wake, both for sensing and charging purposes, but if this configuration is unavoidable, a lower potential servicer is best when the target is in the servicer's wake. A conservative conclusion when no current is detected in this configuration may be that the target has been charged highly negatively in the wake of the servicer.

B. Feasibility results

Based on Sec. V A, the best case scenario for sensing is a 0.2 λ_D length 50 V servicer in the target's wake when in a sunlit environment and a 0.2 λ_D length 300 V servicer in the target's wake in an eclipse environment. In both environments, the worst-case scenario is a target in the wake of a 300 V servicer. In any scenario, the detected electron emission current must be large enough to differentiate from the current due to the ambient electrons. An electrostatic analyzer (ESA), such as a retarding potential analyzer (RPA), is proposed to measure the energy and flux of the electron emissions and ambient environment. The resulting measurements can be modeled as discrete energy bins with a width equal to the error in measurements. This is typically denoted as $\Delta E/E$ for electrostatic analyzer type instruments, and the energy resolution $\Delta E/E$ is assumed to be 4%, comparable to the resolution found by Bengtson *et al.*[14] The height of the bins is equal to the total detected current of electrons with energies between the min and max values of the energy bin.

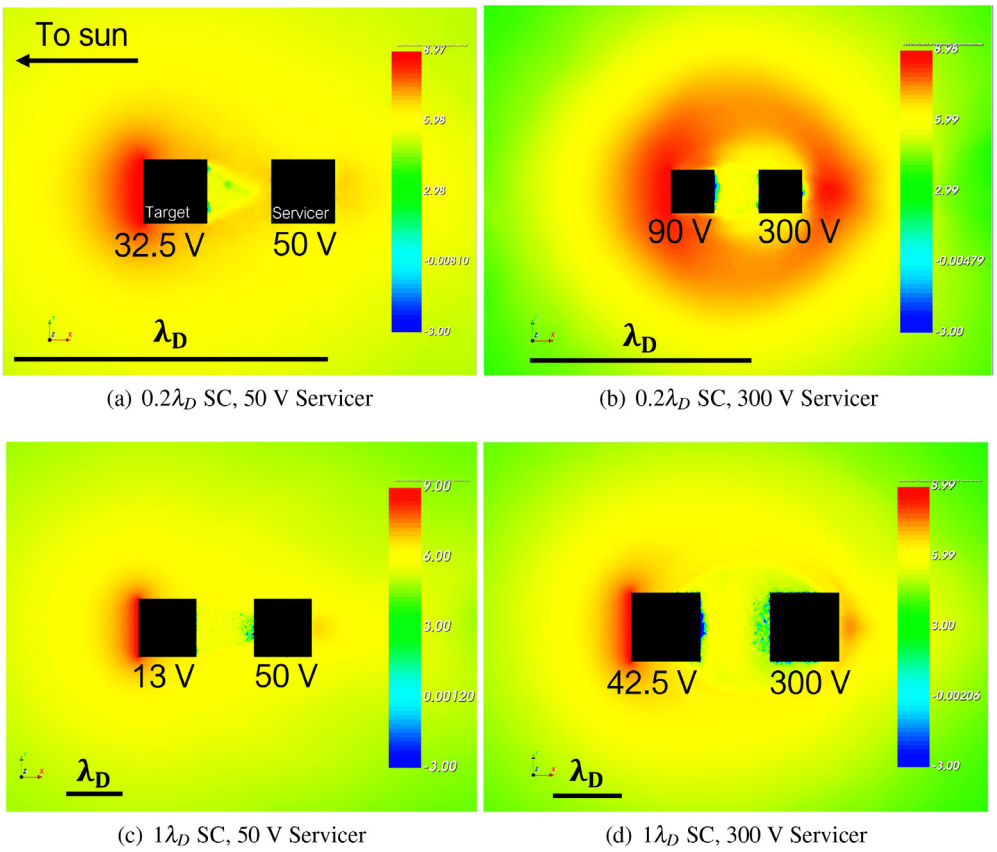

(a) $0.2\lambda_D$ SC, 50 V Servicer (b) $0.2\lambda_D$ SC, 300 V Servicer

(c) $1\lambda_D$ SC, 50 V Servicer (d) $1\lambda_D$ SC, 300 V Servicer

FIG. 11. Log_{10} of the photoelectron density about a target (left) and servicer (right) for the servicer in the target's wake.

The total measured ambient electron current $I_{e,\text{tot}}$ can be taken from SPIS and multiplied by the Maxwellian energy distribution function $f_E(E)$ to model the measured electron distribution $[I_e(E) = I_{e,\text{tot}} f_e(E)]$. The Maxwellian energy distribution function is[1]

$$f_e(E) = \frac{2}{\sqrt{\pi} T_e^{3/2}} \sqrt{E} \exp\left(\frac{-E}{T_e}\right), \tag{8}$$

where E is the energy in eV. The detected electrons are accelerated by the potential of a positively charged servicer, so the spectrum is shifted such that the minimum detected energy is equal to the servicer's surface potential.

Various models exist for the energy distribution of electron emissions $f_{se/ph}(E)$, including the Chung–Everhart model,[101] a Gaussian fit with a logarithmic argument,[102] and a Maxwellian distribution. As mentioned in Sec. III, SPIS models the electron emissions as a Maxwellian distribution with a temperature of 2 eV. To keep the feasibility analysis consistent with the characterization results in SPIS, a Maxwellian distribution is used to model both photoelectron and secondary electron emissions. As mentioned in the introduction, the electron emissions are accelerated away from a negative target and toward a negative servicer such that the energy of the secondary and photoelectron emissions $E_{SE/Ph}$ at detection is

$$E_{SE/Ph}(E) = T_{se,ph} f_{se/ph}(E) + \phi_{\text{ser}} - \phi_{\text{tar}}, \tag{9}$$

where ϕ_{ser} and ϕ_{tar} are the servicer and target's potential, respectively. If the target is charged positively, it is assumed that the electron emissions leave the target with negligible initial energy, or $\phi_{\text{tar}} \approx 0$ V. The detected ambient electron and electron emission currents are then superimposed to model the complete detected spectrum.

Figure 13(a) is an example of measurements in a scenario where the target is in the wake of a 0 V servicer in the dayside environment. As shown, the bin with the secondary electron emissions is over 200 μA larger than the next tallest bin, indicating that the electron emissions can be distinguished from the ambient environment. Figure 13(b) is an example of a best-case setup where a 300 V servicer is in the wake of the target in the eclipse environment. The target is charged positively, so the electron emissions are captured in the first energy bin, which is over twice as large as the next bin. In addition, the horizontal line in the first bin indicates an initial measurement of the environment without secondary electron emissions, which is about half the size of the bin when the electron emissions are detected. Therefore, the electron emissions can be differentiated from the environment in both tested cases.

VI. CONCLUSION

Knowledge of a neighboring spacecraft's potential can be used to avoid electrostatic discharges when docking, account for electrostatic

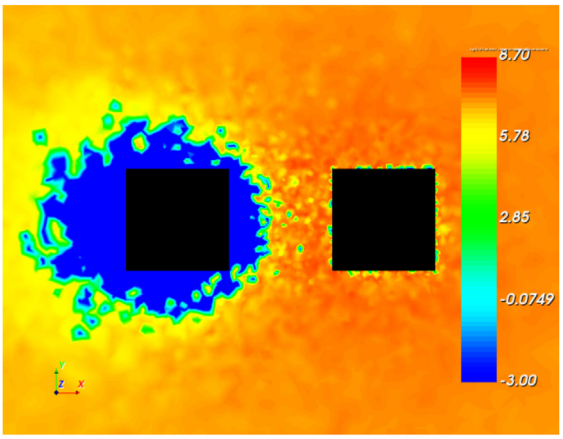

(a) Electron density

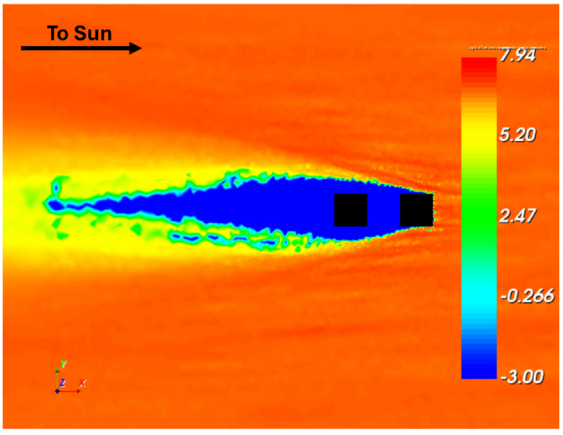

(b) Ion density

FIG. 12. Log_{10} of the electron (top) and ion (bottom) densities about a 0.2 λ_D, 300 V servicer (right) and −70 V target (left) in the solar wind sunlit region.

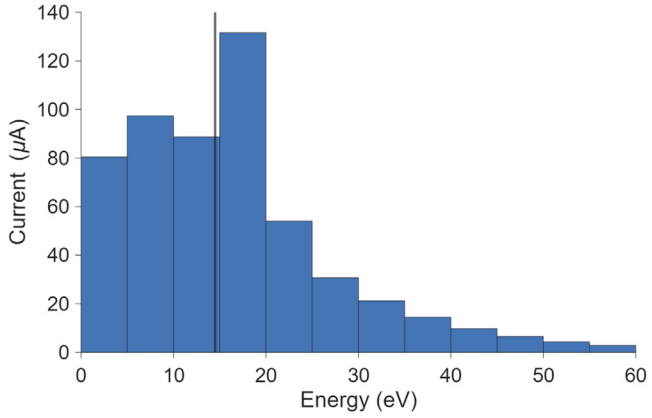

(a) 0 V Servicer, -14.5 V target, 1λ_D SC width, target in wake

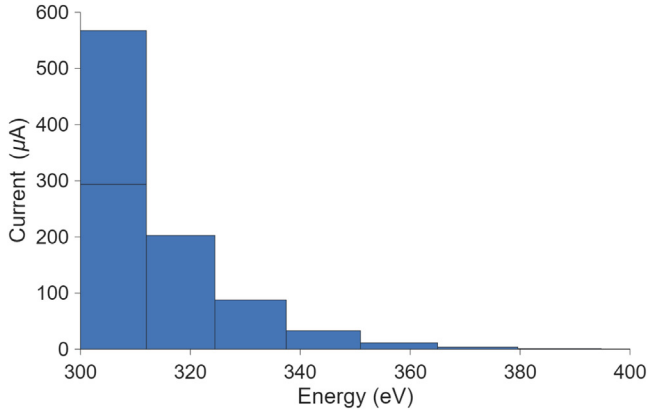

(b) 300 V servicer, 6.5 V target, 0.2λ_D SC width, servicer in wake

FIG. 13. Simulated ESA measurements for various sensing scenarios. The vertical line indicates the expected arrival energy of electron emissions from the target.

forces and torques, and provide insight into lunar dust contamination. However, barriers due to spacecraft wakes and nonmonotonic sheaths can prevent electron emissions used for touchless potential sensing from being detected. The barriers are characterized by spacecraft of varying widths and potentials in solar wind dayside and eclipse plasma. It is found that barriers can form when the spacecraft width is half the Debye length and are largest when the spacecraft is uncharged. Barriers due to nonmonotonic sheaths persist as the spacecraft charges more negatively, while barriers due to the spacecraft wake persist as the spacecraft charges more positive.

Simulations of passive potential sensing when barriers are expected ($W_{SC} = 1\lambda_D$) and not expected ($W_{SC} = 0.2\lambda_D$) reveal that fewer electron emissions leave a target when barriers are expected, and the detected current density is lower. However, sensing is not fully prevented, as a positively charged servicer is able to draw electron emissions through anticipated barrier formations, such as the target's wake. When the target is not in the servicer's wake, a 50 V servicer is best for using photoelectrons for sensing, and a 300 V servicer is best for using secondary electrons for sensing. When the target is in the servicer's wake, a highly positive servicer can begin to enhance the wake formation, leading to less ion current to the target and a highly negative surface potential. This then prevents ambient electrons from impacting the target and generating electron emissions. Therefore, placing the target in the servicer's wake should be avoided for both charging and sensing purpose, and the servicer's potential should be minimized if this configuration is necessary. It is likely that other constraints are present during proximity operations that can prevent the servicer from positioning itself to detect the target's potential. Regardless, these results can be utilized to position the servicer in a way to detect the target's potential prior to docking, or inform the operators why electron emission measurements from the target may not be detected during proximity operations.

The electron emissions passively generated from a target can be differentiated from the environment, showing that passive potential sensing through barriers in cislunar space can be conducted to achieve both scientific and safety goals.

ACKNOWLEDGMENTS

This work is supported by a NASA Space Technology Graduate Research Opportunity Grant No. 80NSSC22K1175 and

the U.S. Air Force Office of Scientific Research under grant FA9550-23-S-0570. The authors would like to thank Dr. Emily Willis for her advice on SPIS simulation techniques.

AUTHOR DECLARATIONS

Conflict of Interest

The authors have no conflicts to disclose.

Author Contributions

K. Champion: Conceptualization (lead); Data curation (lead); Formal analysis (lead); Funding acquisition (supporting); Investigation (lead); Methodology (lead); Software (lead); Validation (lead); Visualization (lead); Writing – original draft (lead); Writing – review & editing (equal). **H. Schaub:** Conceptualization (supporting); Funding acquisition (lead); Investigation (supporting); Methodology (supporting); Supervision (lead); Writing – review & editing (equal).

DATA AVAILABILITY

The data that support the findings of this study are available from the corresponding author upon reasonable request.

REFERENCES

[1]S. T. Lai, *Fundamentals of Spacecraft Charging: Spacecraft Interactions with Space Plasmas* (Princeton University Press, 2012).
[2]K. Balmain, "Arc propagation, emission and damage on spacecraft dielectrics: A review," J. Electrostat. **20**, 95–108 (1987).
[3]J. A. Roth, "Electrostatic discharge in spacecraft materials," Ph.D. thesis (Utah State University, 2009).
[4]S. T. Lai, K. Cahoy, W. Lohmeyer, A. Carlton, R. Aniceto, and J. Minow, "Chapter 16—Deep dielectric charging and spacecraft anomalies," in *Extreme Events in Geospace*, edited by N. Buzulukova (Elsevier, 2018), pp. 419–432.
[5]Y. Xiangqian, C. Hongfei, Z. Qiugang, W. Jianzhao, S. Weihong, Z. Hong, Z. Jiqing, Z. Weiying, C. Zhe, S. Sipei *et al.*, "Mitigating deep dielectric charging effects in space," IEEE Trans. Nucl. Sci. **64**, 2822–2828 (2017).
[6]X. Yu, S. Song, H. Chen, Y. Qu, H. Zou, Q. Zong, W. Shi, J. Zou, W. Zhong, H. Xiang *et al.*, "Monitoring deep dielectric charging effects in space," IEEE Trans. Nucl. Sci. **67**, 716–721 (2020).
[7]J. Wang, P. Leung, H. Garrett, and G. Murphy, "Multibody-plasma interactions-charging in the wake," J. Spacecr. Rockets **31**, 889–894 (1994).
[8]M. McCollum, E. Willis, and A. Diekmann, "Artemis IV docking in radiation belt charging environment," in *Applied Space Environments Conference 2023* (National Aeronautics and Space Administration, Huntsville, AL, 2023).
[9]E. Willis, A. Diekmann, and M. Guy, "Plasma charging of crewed spacecraft in lunar orbit," in *Space Environment Engineering and Science Applications Workshop* (Johns Hopkins University Applied Physics Laboratory, Laurel, MD, 2022).
[10]K. T. H. Wilson, Á. R. Calvo, and H. Schaub, "Constrained guidance for spacecraft proximity operations under electrostatic perturbations," J. Spacecr. Rockets **59**, 1304–1316 (2022).
[11]R. G. Lee, E. S. Worthy, E. M. Willis, G. L. Brown, F. Cipriani, and D. C. Barker, "Development of a comprehensive physics-based model for study of NASA gateway lunar dust contamination," Acta Astronaut. **210**, 616–626 (2023).
[12]M. Bengtson, J. Hughes, and H. Schaub, "Prospects and challenges for touchless sensing of spacecraft electrostatic potential using electrons," IEEE Trans. Plasma Sci. **47**, 3673–3681 (2019).
[13]M. T. Bengtson and H. Schaub, "Electron-based touchless potential sensing of shape primitives and differentially-charged spacecraft," J. Spacecr. Rockets **58**, 1847–1857 (2021).
[14]M. T. Bengtson, K. T. Wilson, and H. Schaub, "Experimental results of electron method for remote spacecraft charge sensing," Space Weather **18**, 1–12, https://doi.org/10.1029/2019sw002341 (2020).
[15]Á. Romero Calvo, J. Hammerl, and H. Schaub, "Touchless potential sensing of complex differentially-charged shapes using secondary electrons," AIAA J. Spacecr. Rockets **59**, 1623–1633 (2022).
[16]K. T. H. Wilson and H. Schaub, "X-ray spectroscopy for electrostatic potential and material determination of space objects," IEEE Trans. Plasma Sci. **47**, 3858–3866 (2019).
[17]K. T. H. Wilson, M. Bengtson, and H. Schaub, "X-ray spectroscopic determination of electrostatic potential and material composition for spacecraft: Experimental results," Space Weather **18**, 1–10, https://doi.org/10.1029/2019sw002342 (2020).
[18]J. Hammerl, A. López, Á. R. Calvo, and H. Schaub, "Touchless potential sensing of differentially charged spacecraft using x-rays," J. Spacecr. Rockets **60**, 648–658 (2023).
[19]Á. Romero Calvo, K. Champion, and H. Schaub, "Enabling ultraviolet lasers for touchless spacecraft potential sensing," IEEE Trans. Plasma Sci. **51**, 2468–2481 (2023).
[20]K. T. H. Wilson, J. Hammerl, and H. Schaub, "Using plasma-induced x-ray emission to estimate electrostatic potentials on nearby space objects," J. Spacecr. Rockets **59**, 1402–1405 (2022).
[21]A. Poppe, J. S. Halekas, and M. Horányi, "Negative potentials above the dayside lunar surface in the terrestrial plasma sheet: Evidence of non-monotonic potentials," Geophys. Res. Lett. **38**, L02103, https://doi.org/10.1029/2010gl046119 (2011).
[22]J. S. Halekas, G. T. Delory, R. P. Lin, T. J. Stubbs, and W. M. Farrell, "Lunar Prospector observations of the electrostatic potential of the lunar surface and its response to incident currents," J. Geophys. Res. **113**, A09102, https://doi.org/10.1029/2008ja013194 (2008).
[23]S. T. Lai and C. Miller, "Retarding potential analyzer: Principles, designs, and space applications," AIP Adv. **10**, 095324 (2020).
[24]R. Schmidt, H. Arends, A. Pedersen, F. Rüdenauer, M. Fehringer, B. T. Narheim, R. Svenes, K. Kvernsveen, K. Tsuruda, T. Mukai, H. Hayakawa, and M. Nakamura, "Results from active spacecraft potential control on the geotail spacecraft," J. Geophys. Res. **100**, 17253–17259, https://doi.org/10.1029/95JA01552 (1995).
[25]L. Goembel and J. P. Doering, "Instrument for measuring spacecraft potential," J. Spacecr. Rockets **35**, 66–72 (1998).
[26]See https://www.intuitivemachines.com/im-1 for "Intuitive Machine's Odysseus Spacecraft Mission Milestones and Overview" (accessed August 15, 2025).
[27]S. Mathavaraj and K. Negi, "Chandrayaan-3 trajectory design: Injection to successful landing," J. Spacecr. Rockets **62**, 159–166 (2025).
[28]C. Li, H. Hu, M. Yang, J. Liu, Q. Zhou, X. Ren, B. Liu, D. Liu, X. Zeng, W. Zuo, G. Zhang, H. Zhang, S. Yang, Q. Wang, X. Deng, X. Gao, Y. Su, W. Wen, and Z. Ouyang, "Nature of the lunar far-side samples returned by the Chang'E-6 mission," Natl. Sci. Rev. **11**, nwae328 (2024).
[29]S. Ueda, T. Ito, and S. Sakai, "A study on guidance technique for precise lunar landing," in Proceedings of 31st ISTS, 2017.
[30]S. Creech, J. Guidi, and D. Elburn, "Artemis: An overview of NASA's activities to return humans to the moon," in *IEEE Aerospace Conference (AERO)* (IEEE, 2022), pp. 1–7.
[31]K. Champion and H. Schaub, "Electrostatic potential shielding in representative cislunar regions," IEEE Trans. Plasma Sci. **51**, 2482–2500 (2023).
[32]K. A. Anderson, L. M. Chase, R. P. Lin, J. E. McCoy, and R. E. McGuire, "Solar-wind and interplanetary electron measurements on the Apollo 15 subsatellite," J. Geophys. Res. **77**, 4611–4626, https://doi.org/10.1029/JA077i025p04611 (1972).
[33]E. Zinner, R. Walker, J. Borg, and M. Maurette, "Measurement of heavy solar wind particles during the Apollo 17 mission," in *Conference on Solar Wind Three 3* (Non Mentionne, 1974), pp. 27–32.
[34]J. Geiss, P. Eberhardt, F. Bühler, J. Meister, and P. Signer, "Apollo 11 and 12 solar wind composition experiments: Fluxes of He and Ne isotopes," J. Geophys. Res. **75**, 5972–5979, https://doi.org/10.1029/JA075i031p05972 (1970).
[35]K. Ogilvie and M. Desch, "The wind spacecraft and its early scientific results," Adv. Space Res. **20**, 559–568 (1997).
[36]R. Vondrak, J. Keller, G. Chin, and J. Garvin, "Lunar reconnaissance orbiter (LRO): Observations for lunar exploration and science," Space Sci. Rev. **150**, 7–22 (2010).

[37]V. Angelopoulos, "The ARTEMIS mission," Space Sci. Rev. **165**, 3–25 (2011).
[38]F. B. Leahy, "SLS-SPEC-159, cross-program design specification for natural environments (DSNE)," No. SLS-SPEC-159 (National Aeronautics and Space Administration, 2021).
[39]K. W. Ogilvie and M. A. Coplan, "Solar wind composition," Rev. Geophys. **33**, 615–622, https://doi.org/10.1029/95RG00122 (1995).
[40]A. J. Hundhausen, "Composition and dynamics of the solar wind plasma," Rev. Geophys. **8**, 729–811, https://doi.org/10.1029/RG008i004p00729 (1970).
[41]S. J. Bame, J. R. Asbridge, H. E. Felthauser, E. W. Hones, and I. B. Strong, "Characteristics of the plasma sheet in the Earth's magnetotail," J. Geophys. Res. **72**, 113–129, https://doi.org/10.1029/JZ072i001p00113 (1967).
[42]S. Haaland, B. Lybekk, K. Svenes, A. Pedersen, M. Förster, H. Vaith, and R. Torbert, "Plasma transport in the magnetotail lobes," Ann. Geophys. **27**, 3577–3590 (2009).
[43]E. Kallio and G. Facskó, "Properties of plasma near the moon in the magnetotail," Planet. Space Sci. **115**, 69–76 (2015).
[44]E. A. Lucek, D. Constantinescu, M. L. Goldstein, J. Pickett, J. L. Pinçon, F. Sahraoui, R. A. Treumann, and S. N. Walker, "The magnetosheath," Space Sci. Rev. **118**, 95–152 (2005).
[45]J. E. Borovsky and J. A. Valdivia, "The Earth's magnetosphere: A systems science overview and assessment," Surv. Geophys. **39**, 817–859 (2018).
[46]N. Y. Ganushkina, M. W. Liemohn, and S. Dubyagin, "Current systems in the Earth's magnetosphere," Rev. Geophys. **56**, 309–332, https://doi.org/10.1002/2017RG000590 (2018).
[47]J. A. Ratcliffe, *An Introduction to Ionosphere and Magnetosphere* (CUP Archive, 1972).
[48]J. Halekas, Y. Saito, G. Delory, and W. Farrell, "New views of the lunar plasma environment," Planet. Space Sci. **59**, 1681–1694 (2011).
[49]J. Wang and D. Hastings, "Ionospheric plasma flow over large high-voltage space platforms. I: Ion-plasma–time scale interactions of a plate at zero angle of attack," Phys. Fluids B **4**, 1597–1614 (1992).
[50]J. Wang and D. Hastings, "Ionospheric plasma flow over large high-voltage space platforms. II: The formation and structure of plasma wake," Phys. Fluids B **4**, 1615–1629 (1992).
[51]Y. Hu and J. Wang, "Plasma wake simulation for charged space platforms: Fully kinetic PIC versus hybrid PIC," IEEE Trans. Plasma Sci. **47**, 3731–3738 (2019).
[52]W. Miloch, V. Yaroshenko, S. Vladimirov, H. Pécseli, and J. Trulsen, "Spacecraft charging in flowing plasmas; numerical simulations," J. Phys.: Conf. Ser. **370**, 012004 (2012).
[53]A. Sjogren, A. I. Eriksson, and C. M. Cully, "Simulation of potential measurements around a photoemitting spacecraft in a flowing plasma," IEEE Trans. Plasma Sci. **40**, 1257–1261 (2012).
[54]Y. Miyake, C. Cully, H. Usui, and H. Nakashima, "Plasma particle simulations of wake formation behind a spacecraft with thin wire booms," J. Geophys. Res. **118**, 5681–5694, https://doi.org/10.1002/jgra.50543 (2013).
[55]R. Biasca and J. Wang, "Ion current collection in spacecraft wakes," Phys. Plasmas **2**, 280–288 (1995).
[56]J. Maxwell and H. Schaub, "Low Earth orbit plasma wake shaping and applications to on-orbit proximity operations," IEEE Trans. Plasma Sci. **47**, 4760–4769 (2019).
[57]W. Oran, U. Samir, N. H. Stone, and E. Fontheeim, "Laboratory observations of electron temperature in the wake of a sphere in a streaming plasma," Planet. Space Sci. **23**, 1081–1083 (1975).
[58]S. Raychaudhuri, J. Hill, H. Y. Chang, E. K. Tsikis, and K. E. Lonngren, "An experiment on the plasma expansion into a wake," Phys. Fluids **29**, 289–293 (1986).
[59]K. Svencs and J. Trøim, "Laboratory simulation of vehicle-plasma interaction in low Earth orbit," Planet. Space Sci. **42**, 81–94 (1994).
[60]S. Hester and A. A. Sonin, "A laboratory study of the wakes of ionospheric satellites," AIAA J. **8**, 1090–1098 (1970).
[61]K. Champion and H. Schaub, "Electrostatic lenses for laboratory spacecraft wake generation," IEEE Trans. Plasma Sci. **53**, 649–660 (2025).
[62]C. Enloe, D. Cooke, S. Meassick, C. Chan, and M. Tautz, "Ion collection in a spacecraft wake: Laboratory simulations," J. Geophys. Res. **98**, 13635–13644, https://doi.org/10.1029/93JA01191 (1993).
[63]M. André, A. I. Eriksson, Y. V. Khotyaintsev, and S. Toledo-Redondo, "The spacecraft wake: Interference with electric field observations and a possibility to detect cold ions," J. Geophys. Res. **126**, e2021JA029493, https://doi.org/10.1029/2021JA029493 (2021).
[64]W. Yu, J. Wang, and K. Chou, "Laboratory measurement of lunar regolith simulant surface charging in a localized plasma wake," IEEE Trans. Plasma Sci. **43**, 4175–4181 (2015).
[65]K. Champion and H. Schaub, "Feasibility of cislunar spacecraft wake generation," in *AIAA SciTech* (AIAA, Maryland, 2023).
[66]T. Burinskaya, "Non-monotonic potentials above the day-side lunar surface exposed to the solar radiation," Planet. Space Sci. **115**, 64–68 (2015).
[67]D. Han, J. J. Wang, and X. He, "Immersed finite element particle-in-cell simulations of plasma charging at the lunar terminator," J. Spacecr. Rockets **55**, 1490–1497 (2018).
[68]S. L. G. Hess, P. Sarrailh, J.-C. Matéo-Vélez, B. Jeanty-Ruard, F. Cipriani, J. Forest, A. Hilgers, F. Honary, B. Thiébault, S. R. Marple, and D. Rodgers, "New SPIS capabilities to simulate dust electrostatic charging, transport, and contamination of lunar probes," IEEE Trans. Plasma Sci. **43**, 2799–2807 (2015).
[69]Z. Huang and J. Wang, "Modeling lunar surface charging under space weather conditions derived from the Artemis and Omni data," IEEE Trans. Plasma Sci. **51**, 2515 (2023).
[70]J. Wang and Z. Huang, "Multiscale numerical simulations of plasma charging effects for an astronaut at the lunar terminator," IEEE Trans. Plasma Sci. **51**, 2561–2570 (2023).
[71]A. I. Eriksson, Y. Khotyaintsev, and P.-A. Lindqvist, "Spacecraft wakes in the solar wind," in Proceedings of the 10th Spacecraft Charging Technology Conference, 2007.
[72]E. Engwall, A. I. Eriksson, M. André, I. Dandouras, G. Paschmann, J. Quinn, and K. Torkar, "Low-energy (order 10 eV) ion flow in the magnetotail lobes inferred from spacecraft wake observations," Geophys. Res. Lett. **33**, L06110, https://doi.org/10.1029/2005gl025179 (2006).
[73]E. Engwall, A. I. Eriksson, and J. Forest, "Wake formation behind positively charged spacecraft in flowing tenuous plasmas," Phys. Plasmas **13**, 062904 (2006).
[74]S. Guillemant, V. Génot, J.-C. M. Velez, P. Sarrailh, A. Hilgers, and P. Louarn, "Simulation study of spacecraft electrostatic sheath changes with the heliocentric distances from 0.044 to 1 au," IEEE Trans. Plasma Sci. **41**, 3338–3348 (2013).
[75]G. Hobbs and J. Wesson, "Heat flow through a Langmuir sheath in the presence of electron emission," Plasma Phys. **9**, 85 (1967).
[76]S. Guillemant, V. Génot, J.-C. Matéo-Vélez, R. Ergun, and P. Louarn, "Solar wind plasma interaction with Solar Probe Plus spacecraft," Ann. Geophys. **30**, 1075–1092 (2012).
[77]J. Deca, G. Lapenta, R. Marchand, and S. Markidis, "Spacecraft charging analysis with the implicit particle-in-cell code iPic3D," Phys. Plasmas **20**, 102902 (2013).
[78]R. E. Ergun, D. M. Malaspina, S. D. Bale, J. P. McFadden, D. E. Larson, F. S. Mozer, N. Meyer-Vernet, M. Maksimovic, P. J. Kellogg, and J. R. Wygant, "Spacecraft charging and ion wake formation in the near-Sun environment," Phys. Plasmas **17**, 072903 (2010).
[79]H. Zhao, R. Schmidt, C. Escoubet, K. Torkar, and W. Riedler, "Self-consistent determination of the electrostatic potential barrier due to the photoelectron sheath near a spacecraft," J. Geophys. Res. **101**, 15653–15659, https://doi.org/10.1029/96JA00322 (1996).
[80]X. Wang, H.-W. Hsu, and M. Horányi, "Identification of when a Langmuir probe is in the sheath of a spacecraft: The effects of secondary electron emission from the probe," J. Geophys. Res. **120**, 2428–2437, https://doi.org/10.1002/2014JA020624 (2015).
[81]J. Zhao, X. Wei, X. Du, X. He, and D. Han, "Photoelectron sheath and plasma charging on the lunar surface: Semianalytic solutions and fully-kinetic particle-in-cell simulations," IEEE Trans. Plasma Sci. **49**, 3036–3050 (2021).
[82]T. Sana and S. Mishra, "Plasma sheath around Chandrayaan-3 landing site: A case study," Planet. Sci. J. **4**, 158 (2023).
[83]X. Wang, J. Pilewskie, H.-W. Hsu, and M. Horányi, "Plasma potential in the sheaths of electron-emitting surfaces in space," Geophys. Res. Lett. **43**, 525–531, https://doi.org/10.1002/2015GL067175 (2016).

[84]V. T. Gurovich, J. Gleizer, Y. Bliokh, and Y. E. Krasik, "Potential distribution in an ion sheath of non-Maxwellian plasma," Phys. Plasmas **13**, 073506 (2006).
[85]U. Isensee and H. Maassberg, "Particle-in-cell simulation of the plasma environment of a spacecraft in the solar wind," Adv. Space Res. **1**, 413–416 (1981).
[86]P. Sarrailh, J.-C. Matéo-Vélez, S. L. G. Hess, J.-F. Roussel, B. Thiébault, J. Forest, B. Jeanty-Ruard, A. Hilgers, D. Rodgers, F. Cipriani, and D. Payan, "SPIS 5: New modeling capabilities and methods for scientific missions," IEEE Trans. Plasma Sci. **43**, 2789–2798 (2015).
[87]V. A. Davis and M. J. Mandell, "Nascap-2k Version 4.3 Scientific Documentation," Technical Report AFRL-RV-PS-TR-2017-0001 (Leidos, Inc., 2016).
[88]B. Thiebault, B. Jeanty-Ruard, P. Souquet, J. Forest, J.-C. Mateo-Velez, P. Sarrailh, D. Rodgers, A. Hilgers, F. Cipriani, D. Payan *et al.*, "SPIS 5.1: An innovative approach for spacecraft plasma modeling," IEEE Trans. Plasma Sci. **43**, 2782–2788 (2015).
[89]D. Tskhakaya, K. Matyash, R. Schneider, and F. Taccogna, "The particle-in-cell method," Contributions Plasma Phys. **47**, 563–594 (2007).
[90]B. Thiébault, A. Hilgers, E. Sasot, H. Laakso, P. Escoubet, V. Génot, and J. Forest, "Potential barrier in the electrostatic sheath around a magnetospheric spacecraft," J. Geophys. Res. **109**, A12207, https://doi.org/10.1029/2004ja010398 (2004).
[91]J. Bonnell, F. Mozer, G. Delory, A. Hull, R. Ergun, C. Cully, V. Angelopoulos, and P. Harvey, "The electric field instrument (EFI) for THEMIS," Space Sci. Rev. **141**, 303–341 (2009).
[92]E. A. Hogan and H. Schaub, "Impacts of hot space plasma and ion beam emission on electrostatic tractor performance," IEEE Trans. Plasma Sci. **43**, 3115–3129 (2015).
[93]E. Hogan and H. Schaub, "Space weather influence on relative motion control using the touchless electrostatic tractor," J. Astronaut. Sci. **63**, 237–262 (2016).
[94]J. Hammerl and H. Schaub, "Coupled spacecraft charging due to continuous electron beam emission and impact," J. Spacecr. Rockets **61**, 1258–1271 (2024).
[95]W. Riedler, K. Torkar, F. Rüdenauer, M. Fehringer, A. Pedersen, R. Schmidt, R. J. L. Grard, H. Arends, B. T. Narheim, J. Troim, R. Torbert, R. C. Olsen, E. Whipple, R. Goldstein, N. Valavanoglou, and H. Zhao, "Active spacecraft potential control," in *The Cluster and Phoenix Missions*, edited by C. P. Escoubet, C. T. Russell, and R. Schmidt (Springer Netherlands, Dordrecht, 1997), pp. 271–302.
[96]K. Torkar, W. Riedler, C. P. Escoubet, M. Fehringer, R. Schmidt, R. J. L. Grard, H. Arends, F. Rüdenauer, W. Steiger, B. T. Narheim, K. Svenes, R. Torbert, M. André, A. Fazakerley, R. Goldstein, R. C. Olsen, A. Pedersen, E. Whipple, and H. Zhao, "Active spacecraft potential control for cluster—Implementation and first results," Ann. Geophys. **19**, 1289–1302 (2001).
[97]K. Torkar, H. Arends, W. Baumjohann, C. P. Escoubet, A. Fazakerley, M. Fehringer, G. Fremuth, H. Jeszenszky, G. Laky, B. T. Narheim, W. Riedler, F. Rüdenauer, W. Steiger, K. Svenes, and H. Zhao, "Spacecraft potential control for double star," Ann. Geophys. **23**, 2813–2823 (2005).
[98]K. Torkar, R. Nakamura, M. Tajmar, C. Scharlemann, H. Jeszenszky, G. Laky, G. Fremuth, C. Escoubet, and K. Svenes, "Active spacecraft potential control investigation," Space Sci. Rev. **199**, 515–544 (2016).
[99]L. Olano and I. Montero, "Energy spectra of secondary electrons in dielectric materials by charging analysis," Results Phys. **19**, 103456 (2020).
[100]D. R. Lide, *CRC Handbook of Chemistry and Physics*, 84th ed. (CRC Press, 2003).
[101]M. S. Chung and T. E. Everhart, "Simple calculation of energy distribution of low-energy secondary electrons emitted from metals under electron bombardment," J. Appl. Phys. **45**, 707–709 (1974).
[102]J. Scholtz, D. Dijkkamp, and R. Schmitz, "Secondary electron emission properties," Philips J. Res. **50**, 375–389 (1996).